Geophysical Research Letters

Supporting Information for

Subduction Zone Interface Structure within the Southern M_w9.2 1964 Great Alaska Earthquake Asperity: Constraints from Receiver Functions Across a Spatially Dense Node Array

Evans A. Onyango[1]*, Lindsay L. Worthington[1], Brandon Schmandt[1], Geoffrey Abers[2]

[1]Department of Earth and Planetary Sciences, Northrop Hall, 221 Yale Blvd NE, University of New Mexico, Albuquerque, New Mexico 87131, USA.

[2]Department of Earth and Atmospheric Sciences, Cornell University, 112 Hollister Drive, Ithaca, NY, 14853-1504, USA.

Contents of this file

Introduction

This supporting file contains the following figures and table:

Figure S1: Back azimuthal distribution, locations and example of teleseismic earthquakes used for receiver function analysis.
Figure S2: Comparison of near co-located nodal and broadband station waveforms and receiver functions.
Figure S3: Map view of piercing points at 20 km depth.
Figure S4: Simple synthetic test of different LVZ thicknesses, and profile of receiver functions with a Gaussian value of 10 (~4.8 Hz).
Table S1: Teleseismic events selected for this study.
Table S2: One-Dimensional model parameters.

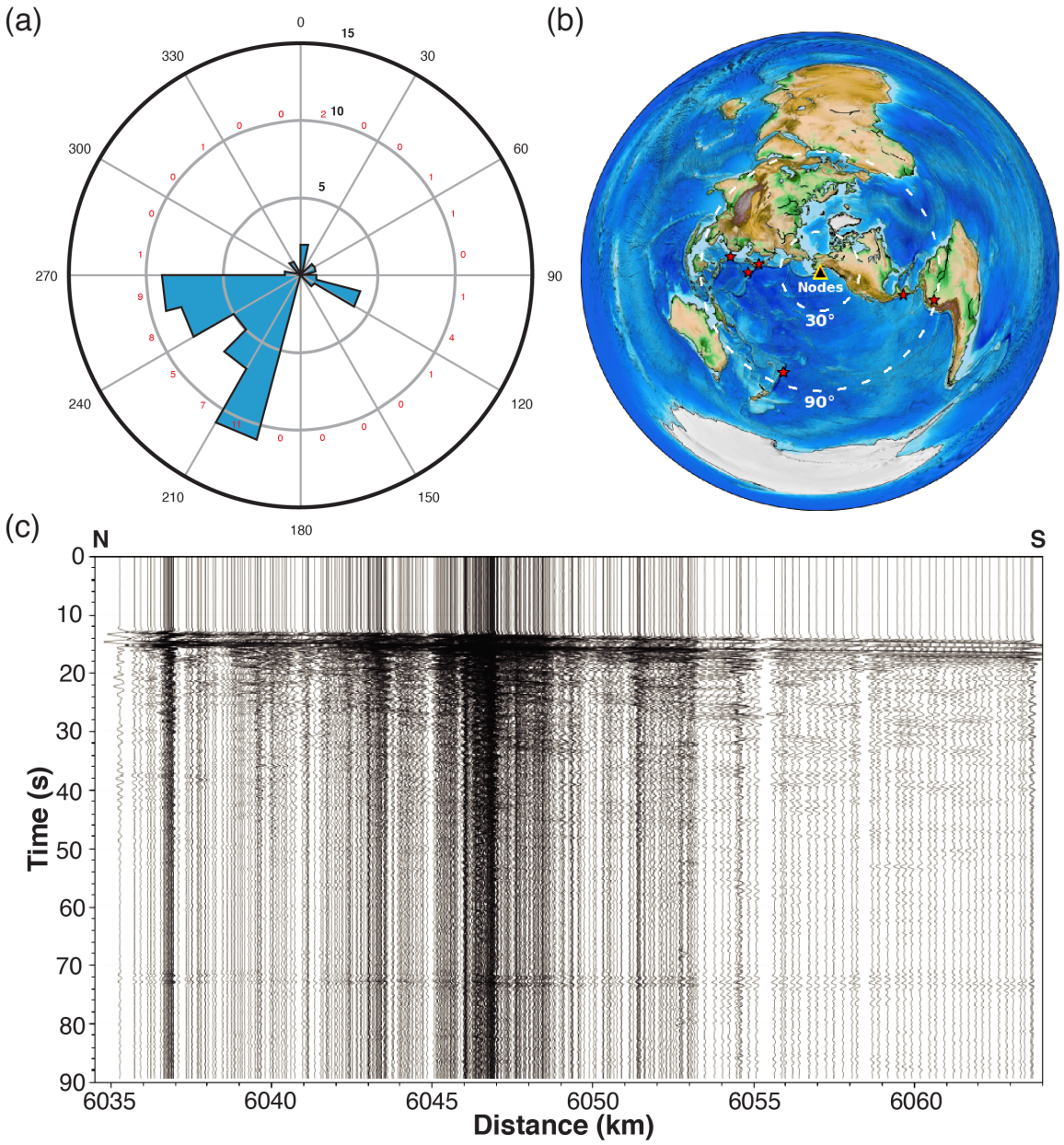

Figure S1. (a) Back azimuthal distribution of teleseismic events >5.0 MW within the 30° – 90° distance window, occurring between May 23, 2019, and June 17, 2019. **(b)** Location of the 7 events selected for receiver function calculation. **(c)** Record section plot of one of the events used for receiver function calculation after instrument response removal, and a bandpass filter (0.2-2 Hz). Amplitudes normalized with

each trace. This Mw 6.3 occurred on 04 June 2019, 04:39:17 UTC at ~430 km depth southeast of Honshu, Japan.

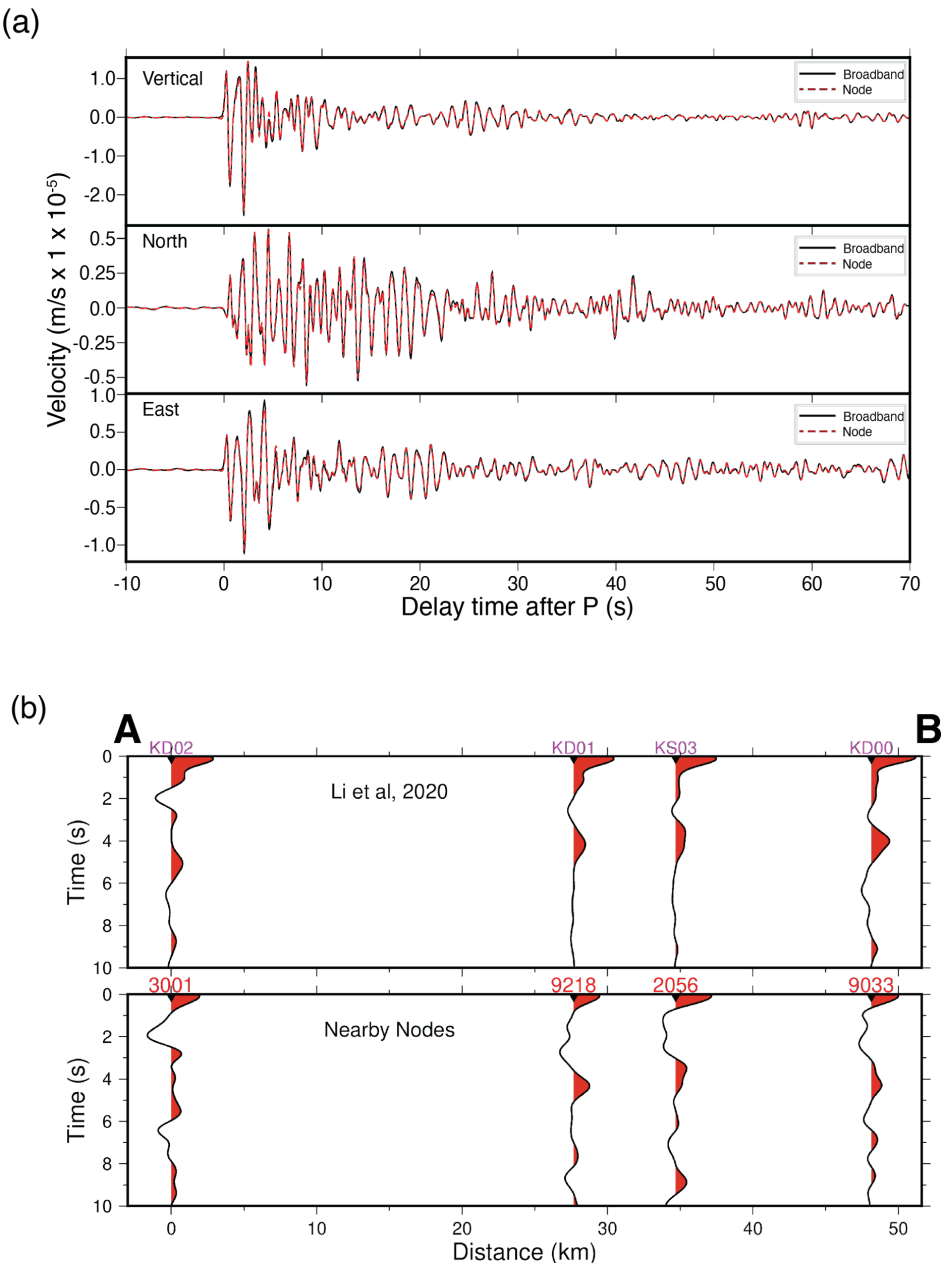

Figure S2. Comparison of near co-located nodal and broadband station waveforms. **(a)** Plots of node station 3001 and broadband station KD02 vertical, east, north component recordings of the 04 June 2019, 04:39:17 UTC Event shown in Figure 2c. **(b)** Plot of the average radial receiver functions for stations KD02, KD01, KS03 and KD00 calculated by Z. Li et al., (2020) projected onto transect AB (top). Plot of the

average radial receiver functions calculated from near-colocated nodal station 3001, 9218, 2056 and 9033 projected onto transect AB.

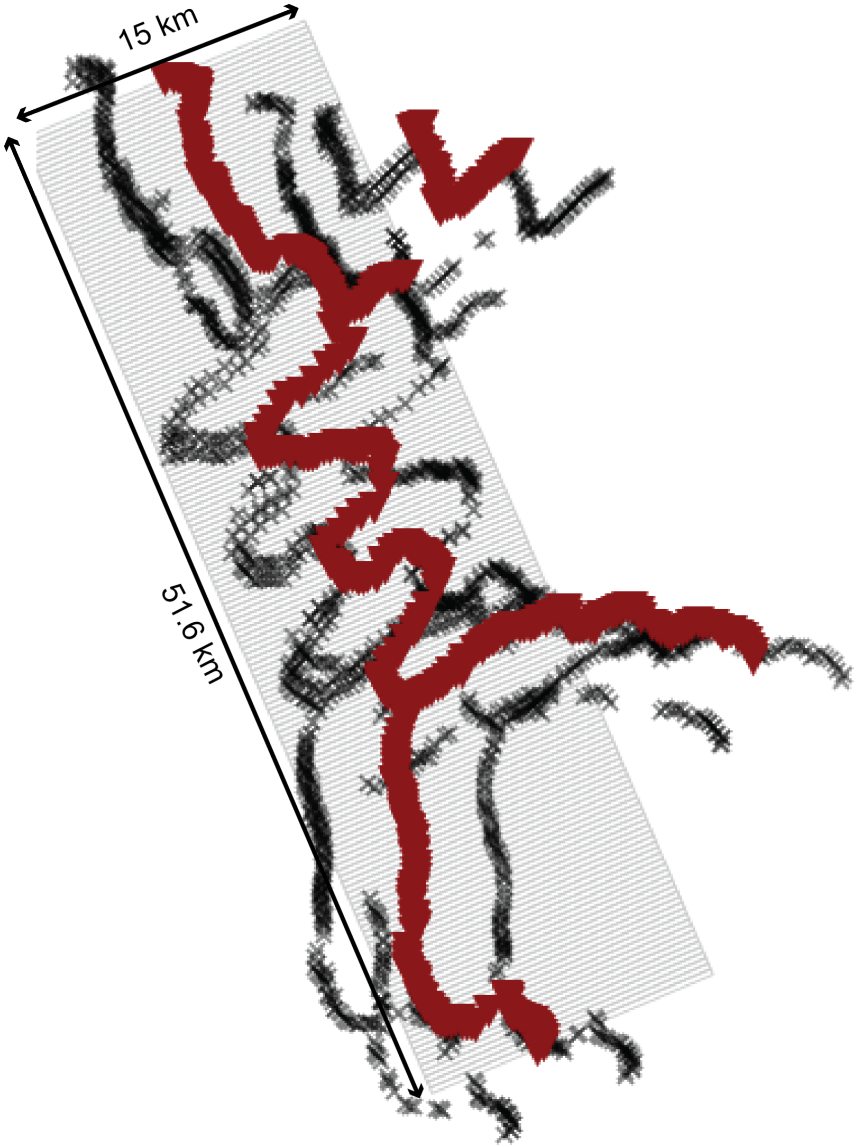

Figure S3. Map of piercing points (black stars) at 20 km depth, and the stations (red inverted triangles) used for common conversion point stacking. The grey rectangles show the position of all the profile boxes used in the stacking.

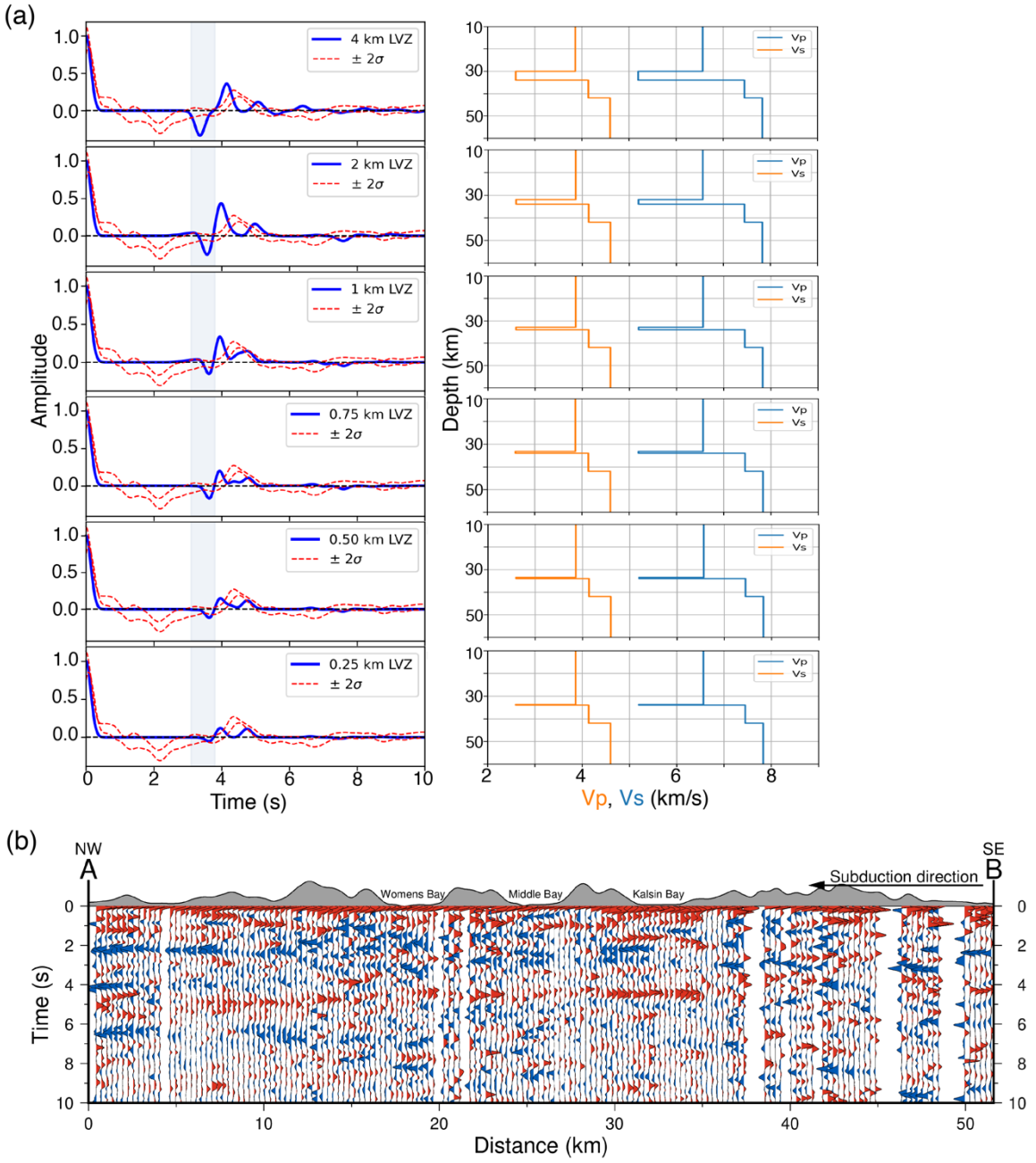

Figure S4. (a) Synthetic tests of 2.5 Hz Ps RFs for models with different LVZ thicknesses. The vertical light blue rectangles in the left panel mark the position of the negative conversion for the 4-km thick LVZ in the top seismogram. The blue lines are synthetic waveforms, and the red dashed lines are the averages of the standard deviations of the field data from Fig.3. **(b)** Moveout-corrected radial receiver functions with a Gaussian value of 10 (~4.8 Hz) stacked by common conversion point.

Time	Latitude	Longitude	Depth	Magnitude
(yyyy/mm/dd hh:mm:ss)	(°)	(°)	(km)	
2019/06/18 13:22:19	38.637	139.4804	12	6.4
2019/06/15 21:56:11	-21.1807	-174.169	13	6.1
2019/06/04 09:46:18	22.8813	121.6704	10	5.6
2019/06/04 04:39:18	29.0623	139.2932	430.3	6.3
2019/06/02 10:36:30	-21.2091	-173.9076	10	6.0
2019/05/26 07:41:15	-5.8132	-75.2775	122.4	8.0
2019/05/30 09:03:29	13.1462	-89.3663	25	6.6

Table S1. Events used in this study.

Model1	V_P **(km/s)**	V_S **(km/s)**	V_P/V_S	**Density (g/cm3)**
Layer1	6.57	3.86	1.7	2.85
Layer2	5.20	2.60	2.0	2.57
Layer3	7.45	4.14	1.8	3.11
Layer4	7.83	4.61	1.7	3.23
Model2	V_P **(km/s)**	V_S **(km/s)**	V_P/V_S	**Density (g/cm3)**
Layer1	6.57	3.75	1.75	2.85
Layer2	7.45	4.14	1.8	3.11
Layer3	7.83	5.22	1.50	3.23
Model3	V_P **(km/s)**	V_S **(km/s)**	V_P/V_S	**Density (g/cm3)**
Layer1	6.57	3.75	1.75	2.85
Layer2	7.83	5.22	1.50	3.23

Table S2. One-Dimensional model parameters.